W-Band Sparse Imaging System Using Frequency Diverse Cavity-Fed Metasurface Antennas

TOMAS ZVOLENSKY[ID], VINAY R. GOWDA[ID], JONAH GOLLUB, (Member, IEEE), DANIEL L. MARKS[ID], AND DAVID R. SMITH

Center of Metamaterials and Integrated Plasmonics, Department of Electrical and Computer Engineering, Duke University, Durham, NC 27708, USA

Corresponding author: Tomas Zvolensky (permaloy@gmail.com)

ABSTRACT We experimentally demonstrate a frequency-diverse, computational imaging system at W-band frequencies utilizing an array of cavity-fed metasurface antennas. Each metasurface antenna consists of a cavity milled from aluminum stock, with an upper plate patterned with a set of radiating slots. As a function of frequency, the metasurface cavities produce a set of spatially diverse radiation patterns that probe the reflectivity distribution of a scene. The antennas are designed to maximize the measurement diversity and hence imaging capacity of the system. The number and distribution of the radiating slots is optimized by balancing the cavity quality factor (Q) and Fourier space coverage. In the experimental realizations, the radiation patterns from each cavity-fed metasurface antenna is first measured using near-field scanning techniques, propagated over the imaging domain, and then stored for use in the image reconstruction step. Comprehensive alignment procedure is implemented to align the measured radiation patterns with regard to the physical position of the cavities. Using a modeling platform, we find excellent agreement between the simulation and experiment, indicating the validity of the calibration and alignment procedures. The scaling of the cavity-fed metasurface antenna represents a key step in the development of alternative high-frequency apertures for imaging and beam-forming applications.

INDEX TERMS W-band, sparse imaging, frequency diverse, metasurface antennas, millimeter waves, resonant cavity.

I. INTRODUCTION

Coherent microwave (1-30 GHz) imaging has proliferated across a host of applications including medical imaging [1], polarimetric target discrimination [2], and especially security screening [3], [4]. Within these fields, evolving technical needs continue to compel the development of higher resolution systems with faster frame rates. Higher resolution can be achieved by operating in the millimeter regime (30-110 GHz) since the diffraction limit is ultimately governed by the operational wavelength. Component cost for millimeter systems, however, is high because of the exotic semiconductor materials, such as SiGe and GaAs, that are necessary to achieve the carrier mobility requisite for operation. This difficulty is compounded for systems requiring fast frame rates, which necessitate many transmitting and receiving components to acquire the necessary measurements swiftly. For example, conventional approaches rely on dense arrays of electronically switched transmitter and receiver elements, as in synthetic aperture radar (SAR) systems [5]–[9]. The hardware costs, and the resulting system complexity remain a considerable impediment to the widespread adoption of W-band imaging systems.

Implementing a sparse multiple input multiple output (MIMO) synthetic aperture is an approach that can reduce hardware requirements. For example, the concept of a W-band imager has been demonstrated with a single transmit/receive pair of open ended waveguides (OEWGs) mechanically translated to synthesize a sparse aperture [10]. Alternative aperture designs have also emerged, including imaging systems that leverage frequency diversity as a means of increasing the number of measurements available from a given aperture [11], [12]. In this approach, scene information is encoded onto a set of pseudo-random radiation modes corresponding to a set of frequencies sampled over the operational bandwidth. Mechanical scanning is replaced by a sparse MIMO approach utilizing large (with respect

to the wavelength) metasurface antennas to cover the necessary spatial frequencies. Image reconstruction from these unconventional measurements is facilitated by computational imaging techniques [13].

Frequency diverse metasurfaces were first designed using subwavelength, resonant metamaterial elements distributed over an aperture, and excited by either a linear or planar waveguide [14]. Subsequently, cavity-backed metasurfaces consisting of simpler, non-resonant metamaterial elements [12] were used; these latter structures had the benefit of lower radiation and resistive losses and improved fabrication tolerance compared with the more geometrically complex subwavelength structures. Frequency diverse apertures can be utilized in conjunction with sparse sampling approaches to achieve a reasonable number of measurement modes within an aperture, but with minimal hardware and substantially simplified radio-frequency (RF) electronics. Recently, it was shown that it is possible to image human-sized targets [15], [16] without mechanical scanning or active components (such as phase shifters, amplifiers and other components typically used in transmit/receive modules). The advantages of utilizing sparse and frequency diverse approaches are even more compelling at high frequencies since the minimal amount of physical hardware required suggests a feasible path to a low-cost, real-time, and high-fidelity imaging system in the millimeter regime.

In this work, a W-band sparse imaging system, based on the cavity backed metasurface design is numerically analyzed and experimentally demonstrated. The results presented here are a continuation of theoretical work presented in [17]. It is demonstrated that utilizing frequency diverse cavities [12] instead of the OEWGs enables increased spatial sampling and ultimately improved imaging.

Replacing the OEWG with cavities introduces field characterization and alignment challenges due to the high Q of the cavities. Because the system relies on maintaining coherency across the aperture [18], any misalignment between the spatial position of a given antenna and its characterized radiated fields results in errors to the forward model, rapidly degrading image reconstruction quality [19]. These challenges are exacerbated at the millimeter wave scale. Nevertheless, a successful alignment approach is demonstrated.

Although the imaging concepts investigated here can be translated to quasi-optical and optical regions, extending the scale of this work beyond millimeter-wave frequencies is beyond the scope of this paper. W-band imagers are especially compelling for security applications where the high resolution is desired for detecting very small threat objects. But, in addition to the hardware challenges at W-band, the computational demands of image reconstruction are significant, especially when imaging large targets such as humans. For example, a typical human-sized target fits within a reconstruction region of interest (ROI) of 1.9 × 1 × 0.26 m [15]. Considering the same ROI and aperture size of 2 × 2 m [15], at the center frequency of W-band, the resolution in cross-range and range is 1 mm

and 4.3 mm respectively. Diffraction limited sampling results in nearly 15 million voxels (or 13 TB of data). This is in contrast to, for example, K-band frequencies (18 - 26.5 GHz) where the discretization of the ROI is still challenging, but computationally feasible (about 90 gigabytes of data that can be calculated on-the-fly using GPU-based parallel processing approaches [20]). Despite the challenges of W-band, various advanced hardware approaches such as [5] have successfully leveraged FPGAs to process the large amounts of data generated by these systems.

The outline of this paper is as follows. In section 2, the forward model used in the reconstruction is described and the motivation for the compressed imaging system is discussed. In section 3, we describe the design of the OEWG MIMO imaging system and experimental imaging results and introduce singular value spectrum as a metric for evaluation of the system performance. In section 4 we present the theory and design of a frequency diverse cavity and discuss the principles governing the optimal cavity design. Section 5 describes the characterization of the OEWG and cavity panels using near field scanning techniques and experimental results from a bistatic imaging system in two configurations: OEWG to cavity, and cavity to cavity. We describe the algorithms used to achieve the necessary alignment and explain the underlying principles of improving the information content of the measurements using frequency diverse cavities.

II. IMAGER DESIGN

An in-house simulation tool, which we refer to here as the Virtualizer, is used to predict the image quality and behavior of a W-band imaging system design. The Virtualizer consists of a set of Matlab functions that model the metasurface aperture, the scattering from objects in the scene, and implements a forward scattering model for image reconstruction.

In the Virtualizer, antennas are conceptually modeled by a distribution of frequency-dependent magnetic dipoles [21]. For example, an OEWG antenna with its low gain radiation, is modeled as a set of closely spaced magnetic dipoles in a rectangular shape, producing the expected cosine current distribution. Further, frequency-dependent magnetic dipoles can be used to simulate radiating metasurfaces, as we discuss below [22]. From the representative dipoles, the dyadic Green's function can then be used to propagate the electromagnetic fields to all points in the scene [23].

A forward model of the radiated fields of the antennas and their scattering dynamics in the scene can then be constructed applying the first Born approximation. This model assumes the incident field is not perturbed, that there is no multipath, and no material dispersion is present. The fields reflected from a volume element (or voxel) are assumed to be the reflectivity associated with that voxel multiplied by the incident field. A measurement at the receiver antenna, g_{ij}, can then be written as

$$g_{ij}(\omega) = \int_V E_i^{Tx}(r, \omega) E_j^{Rx}(r, \omega) f(r) dV + w \quad (1)$$

where E_i^{Tx} and E_j^{Rx} are the *i*-th transmitter and *j*-th receiver electric fields respectively at the scene position *r* and angular frequency ω; *w* is the additive white noise. Eq. (1) defines a single measurement for a transmitter and receiver pair. Discretizing the scene volume into a finite number of diffraction limited voxels, we can write Eq. (1) in the matrix form

$$g = Hf + w \qquad (2)$$

where **H** is a *MxN* matrix composed of *M* measurements and *N* voxels whose components $H_{m,n}=\mathbf{E}(r_n)_m^{Tx}\ \mathbf{E}(r_n)_m^{Rx}$; Here *m* indexes the rows of the **H** distinguishing given pair of Tx, Rx antenna and frequency, r_n is the voxel positions in the scene and **w** is the additive white noise. By solving Eq. (2) it is possible to obtain an estimate of the reflectivity the scene. However, in general **H**, consisting of an under or oversampled set of correlated measurements, is not square or well-conditioned, and thus an inverse is not defined and the solution to Eq. (2) must be approximated. Back-propagation (or, matched filter), in which the Hermitian transpose of **H** is used to compute $f_{est} = H^\dagger g$, provides the simplest and fastest estimate [24], [25] of **f**, while an iterative least squares approach [26] can improve the estimation. As will be discussed further below, the measurement modes of the metasurface antenna tend to be correlated and generally do not provide complete coverage in either real space or Fourier space. For this reason, the scene estimates attempt to find the best solution possible within the subspace spanned by the available measurement modes. The exact solution is unlikely to lie within this subspace, and thus scene estimates have an inherent reconstruction noise level that exists simply due to mode incompleteness.

It has been shown that for a frequency diverse system, the Q of the resonant elements [21] or guided wave structure [11], [15], is a parameter that, in conjunction with the layout of the radiating elements, can be used to predict the imaging performance of the aperture. At microwave frequencies, it is possible to design resonant metasurface elements, such as complimentary electric LC resonators (cELCs), with moderate values of Q, using copper clad printed circuit board (PCB) waveguide based structures [21]. However, at W-band frequencies the reduced metal conductivity, surface roughness, and dielectric losses all significantly reduce the achievable Q-factors for PCB-based structures [27]. Even by leveraging the most advanced low-loss substrates and metal plating techniques the Q can only be increased marginally [28]. As an alternative, we instead use air-filled machined metasurface cavity structures with radiating slots cut in the front surface [12]. This structure naturally leverages the low dielectric loss of air, and hence supports much higher Q values at W-band frequencies than dielectric waveguide structures.

Since the radiation profile of a mode-mixing resonant cavity is highly diverse and not easily analytically predicted [11], we use a near-field scanning technique to characterize the fabricated cavity antennas [29]. The fields are measured and imported in the Virtualizer modeling software as a set of

equivalent dipoles as discussed above [21]. Hence, we can model different system configurations using these realistic, experimentally derived models.

III. OEWG ARRAY IMAGING

Using the Virtualizer, we first modeled an OEWG transmitting array to an OEWG receiver configuration. The system modeling capability allows us to optimize the parameters of the imaging experiment to achieve acceptable image quality within the limited spatial region consisting of a 30×30 cm surface imposed by the scanning stage used (NSI-100V-1x1 near-field antenna scanner stage). The OEWG measurements were modeled as a set of 15 dipoles equidistantly distributed over the surface of the WR-10 waveguide rectangle (2.54×1.27 mm). The number of dipoles was chosen such that the radiation pattern of the array resembles the OEWG performance while not being computationally burdensome. This modeling approach suffices to obtain a qualitative measure of the expected imaging performance; however, we also performed a near field scan of an OEWG to determine the exact radiation pattern with equipment as discussed below. Importing the fields associated with the near-field scan into the Virtualizer software minimizes the error in our forward model.

The fields were scanned at 200 frequency points at each position and imported for both simulation and experimental reconstruction.

The experimental configuration is composed of two W-band extension heads (OML V10VNA2, frequency range 75-110 GHz) with one of them mounted on a moving stage and one fixed and supported by four pillars as shown in Fig. 1a. The extension heads are connected to a Performance Network Analyzer (PNA, Keysight N5222A) acting as a source of base-band signal which is connected to a computer (using a TCP connection) controlling the whole measurement through a Matlab script.

Figures 1b and 1c show the configuration in Fig. 1a in different planes indicated by the coordinate systems. The measurements are done by scanning the head on the moving stage over a rectangular surface with dimension A = 15 cm (each dot of Fig. 1b symbolizes measurement position) and recording the S_{21} parameter. The size of the test targets was chosen based on the SAR resolution limit, which is estimated using formula d = λR/2D, where λ is the wavelength at the center of the bandwidth, R is the distance from the aperture plane to the target (shown in Fig. 1c) and D is the total size of the aperture, see Fig. 1b [7]. In our case, d = 1 mm. Since the calculated limit applies to sparse imaging systems only approximately [25], and the total aperture is not exactly square, we chose the size of the test targets 5 mm.

The three stripe resolution target (Fig. 2a) and five-point square target (Fig. 2c) are imaged using a grid of 121 points as shown in Fig. 1b resulting in M = $121 \times 200 = 24200$ measurements.

Initially, the reconstruction volume was $30 \times 30 \times 50$ mm, but for the sake of rapid reconstruction, we narrowed the
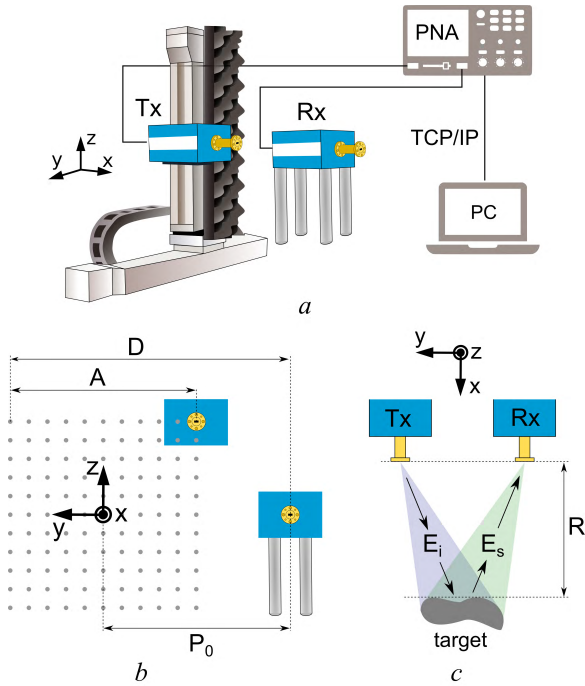
FIGURE 1. *a* An illustration of the experimental setup using two W-band frequency extension heads fed by K-band base-band signal from a Performance Network Analyzer (PNA) and precision linear stage capable of automated scanning in *yz* plane. The transmitting block, Tx, and receiving block, Rx, are shown. *b* A sketch of the synthesized aperture (with 121 scan points) with the Tx head fixed and Rx scanned over a regular grid of points over the aperture A = 15 cm is shown. The Tx head is positioned at P_0 = 18 cm. c A single measurement is the process of detecting the fields E_s scattered by the target, illuminated by the E_i fields transmitted from Tx; R = 15 cm.
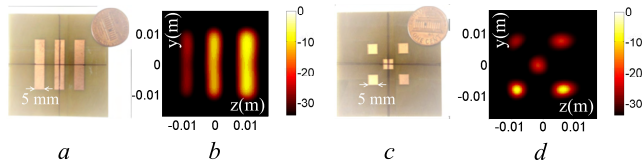

FIGURE 2. *a* Resolution target with 5 mm stripe width, *b* simulation imaging results, *c* squares target with 5 mm size, *d* simulation imaging results. Reconstruction method for all images was matched filter.
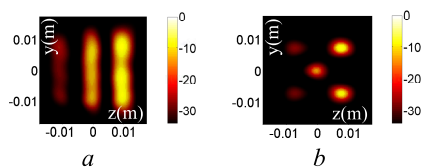

FIGURE 3. *a* Experimental image of resolution target, *b* experimental image of the squares target.

volume to a two-dimensional cross-range slice leaving us with N = 140 × 140 = 19600 pixels. Matched filter was used for image reconstruction, as shown in Figs. 2b, 2d, 3, and 4, together with the target photographs.

The excellent reproduction observed comparing Fig. 2 and 3 indicates precise agreement between simulation and measurement. We note that in this case, no additional
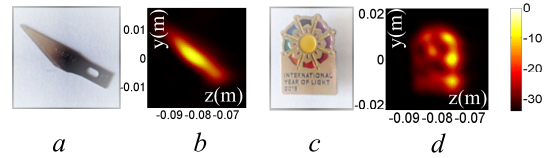
FIGURE 4. *a* Razor target, *b* experimental image of the razor target, *c* badge target, *d* experimental image of the badge target.
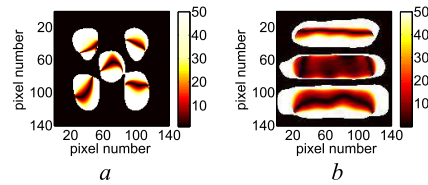
FIGURE 5. *a* 2-D error map for the measurement of the five squares target relative to simulation results in percent *b* 2-D error map for the measurement of the resolution target relative to simulation results in percent.

alignment methodology was necessary to capture the images. The precise grid layout of the transmitter OEWG antennas and their rather simple radiated field profile (i.e., slowly changing phase and amplitude) provide a degree of resilience to error [30] when determining the position of the receiver OEWG antenna positions in image reconstruction calculations. We note that this is not the case for the cavity-based imager we discuss below. The difference between measurement and simulation is quantified by drawing 2-D maps showing the absolute percent error relative to the simulation results in Fig. 5 for both targets. The mean absolute error is 29% for resolution target and 12.6% for five squares target. The error is highest at the edges of the targets because of imperfect alignment of simulated and experimental data and the limits of the forward model used in the simulation tool. Generally, within the capabilities of the simulation tool, we suggest that the experiment and simulation results demonstrate good agreement.

An attempt to image more complex targets resolved the approximate shape of a badge and a razor (see Fig. 4a-d), but the lack of detail suggests that the measurement modes do not contain enough information to fully resolve the scene. This result is not unexpected, since the spacing between measurement locations (over 1 cm) is much larger than the Shannon sampling limit of λ/2 (or roughly 1.6 mm); The cross-range resolution of the imaging system depends on the aperture size and sampling [7]. The radiation pattern of an OEWG is for all practical considerations frequency independent. Thus, the frequency sampling does not contribute to the image fidelity in this experiment.

Tailoring the measurement capacity of the system to the target of interest is a critical design consideration for computational approaches. A useful measure of the non-overlapping information content of a set of measurements is the singular value spectrum. The singular value decomposition (SVD) [30], [31] is a factorization of the measurement

matrix **H** into a product of three matrices $H = USV^T$. Here, **S** is a diagonal matrix of real values organized from largest to smallest; **U** and **V**^{T} are matrices with orthonormal columns.

A flat singular value "spectrum" signifies maximum orthogonality among the measurements, while a decaying spectrum signifies correlation among the measurements. Hence, plotting the singular values spectrum provides a measure of the "information content" of the measurement matrix. The total number of measurements is the number of positions of the Tx antenna multiplied by the number of positions of the Rx antenna and the number of frequency points. Although the resulting number of modes is large, observing the singular value spectrum in Fig. 6, the correlation of the measurement modes causes the decay of the singular values indicating diminishing benefit from the many modes available.
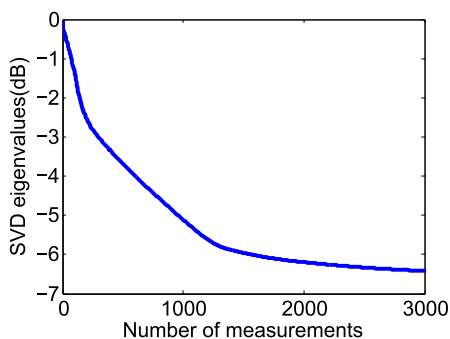

FIGURE 6. Singular value spectrum of the measurement matrix used in the experiment with OEWG antennas.

IV. CAVITY DESIGN

As noted in section 2, resonant high Q cavities are a proven platform for harnessing a set of frequency diverse measurements with high information content [12], [15]. The high Q factor is afforded by using polished air-filled cavities machined from a bulk aluminum block, which minimizes the dielectric and metal losses. The metasurface antenna design process was as follows. First, a *non-radiating cavity* (see Fig. 7a) was simulated in CST Microwave Studio to estimate its Q-factor, determined from the decay time (impulse response) of the fields inside the cavity [31]. The shape of the cavity was chosen to randomize the waveform in the cavity. Therefore no walls are parallel and the saw-tooth pattern on top and bottom wall ensures irregular guided mode structure and thus random far-field patterns with changing frequency, increasing the information value of each radiated mode.

In our case, the Q-factor of the non-radiating cavity was 3500 at 92.5 GHz (center frequency of W-band). The simulated cavity mode is shown in Fig. 7b, and is seen to be highly random. The optimal number of useful radiating slots to be patterned over the aperture can be estimated from [31]:

$$Q > TR\frac{f_c}{B} \quad (3)$$

where Q is the quality factor obtained from full-wave simulation; T and R are the numbers of radiating slots on the
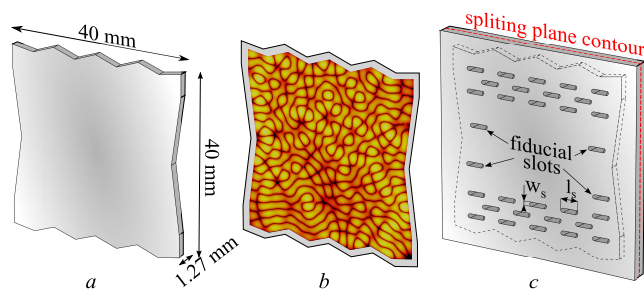

FIGURE 7. *a* The shape of the closed aluminum cavity *b* an example of guided mode E fields at 92.5 GHz *c* a final structure with radiating slots, together with four RF fiducial slots off the regular pattern for alignment purposes and a contour of the splitting plane dividing the cavity into two parts during the fabrication process. The dimensions of the slot are $l_s = 2$ mm and $w_s = 0.14$ mm.
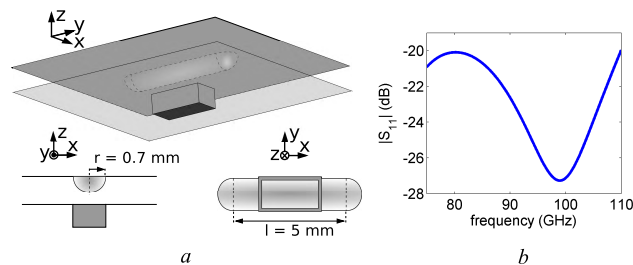

FIGURE 8. *a* The geometry of the WR-10 to parallel plate waveguide transition with dimensions, *b* CST Microwave studio simulation results of input matching of the transition.
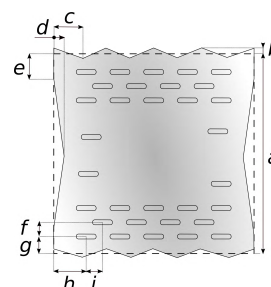

FIGURE 9. The dimensions of the cavity: $a = 40$ mm, $b = 0.35$ mm, $c = 6.2$ mm, $d = 2$ mm, $e = 4.5$ mm, $f = 4$ mm, $g = 4.75$ mm, $h = 5.8$ mm, $i = 4.75$ mm.

Tx and Rx antennas respectively; and, f_c, is the center frequency of the bandwidth, B, utilized (35 GHz).The remaining dimensions of the cavity are shown in Fig. 9.

The loaded cavity Q-factor (Fig. 7c) is estimated by measuring the impulse response of the feed signal, which is the scattering parameter S_{11}. For the closed cavity, the predicted number of useful radiating slots is 36. Since the Q-factor of the cavity decreases with the addition of each new slot, or radiation vector, this number should be the starting point of an iterative design process. After each full-wave simulation, a new Q-factor can be determined and the design and layout updated with the new predicted number of slots (until an equilibrium is achieved). The optimized structure is a balance between the desire for a high Q-factor (supporting more frequency diverse measurement modes), and
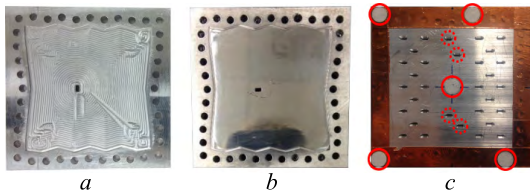
FIGURE 10. The fabricated sample of the cavity *a* before, and *b* after surface polishing which resulted in a two-fold increase of the Q-factor and enabled the use of two hundred frequency points instead of just one hundred. *c* The cavity front with optical (full circles) and RF (dashed circles) fiducials used for alignment.

FIGURE 11. Measured $|S_{11}|$ and η, radiation efficiency of the fabricated cavity. The dashed horizontal line in the efficiency plot is the average efficiency of 40% over the whole bandwidth (75 - 110 GHz).

FIGURE 12. Example of the far-field radiation pattern of fabricated cavity at *a* 75, *b* 90 and *c* 105 GHz. Random radiation pattern at each frequency generates information content of the fields scattered from a target aiding successful image reconstruction.

the contrasting desire for additional slots to maximize the spatial sampling of the aperture and improved antenna radiation efficiency. At W-band, radiated power is a scarce commodity. In order to ensure sufficient signal to noise ratio (SNR) for this first demonstration, we used the initially estimated slot number based on the impulse response of the closed cavity (favoring radiation efficiency over maximizing the Q-factor).
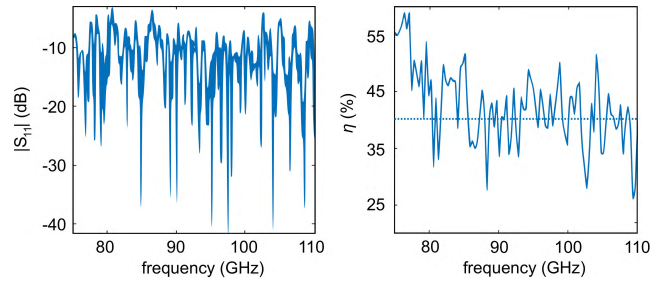
The positions of the slots were set to allow the frequency diverse measurements to optimally sample the accessible k-space of the antenna [31]. The Mills Cross arrangement [30], [31] of radiating elements has been shown to produce minimally redundant sampling (i.e., highly orthogonal radiated modes) and was used in our metasurface cavity design, as shown in Fig. 7c. The cavity is fed via a WR10 waveguide and a mode-matching transition, which emulates the performance of the E-plane waveguide junction [32] with the additional element in the form of matching half cylinder milled into the top wall of the cavity.

The geometry of the transition is shown in Fig. 8a together with its dimensions and input reflection in Fig. 8b indicating matching below -20 dB over the entire observed bandwidth.

The bottom part of the fabricated cavity is shown in Fig. 10a with clearly visible tool-path milling artifacts. In preparation for the experiments, the inner cavity surface was polished with buffing abrasive, increasing the Q-factor of the loaded cavity (Fig. 10c) from 300 to approximately 600. The final cavity surface is almost mirror-like (see Fig. 10b). Based on Eq. (3), 200 frequency points can be used to fully leverage the frequency diversity available and are used in the experiments described in the following section. The $|S_{11}|$ and radiation efficiency of the cavity is shown in Fig. 11. The cavity was designed to have average radiation efficiency $\eta = 80\%$, corresponding to the $|S_{11}|$ of high quality-factor cavity with many resonant points. Due to the surface roughness, which was not accounted for in the simulation, the measured η averaged over the band of operation was 40%. Far-field radiation pattern plots of the cavity at three different frequencies are shown in Fig. 12, demonstrating the random nature of the radiated fields due to the high quality factor.

V. CAVITY IMAGING
As an alternative to the complicated and costly hardware [10] associated with a massive MIMO W-band system for
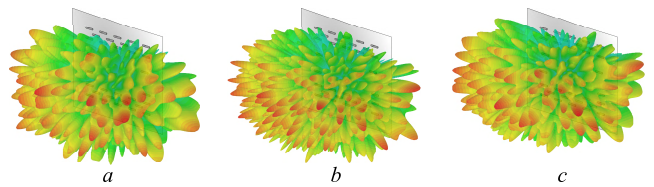
imaging, we utilized the frequency diverse cavity structure [12], [15], developed in section 4, and computational image processing techniques, as described in section 3.

Comparing the singular value spectrum in Fig. 14 of the three experimental setups, i.e., OEWG to OEWG (Fig. 1b), OEWG to cavity (Fig. 13a) and cavity to cavity (Fig. 13b), it becomes evident that the orthogonality of the measurement modes is improved by replacing the OEWG by cavities at the receiver and transmitter positions and leveraging frequency diversity. This improved mode diversity ultimately supports improved image quality as we now discuss.
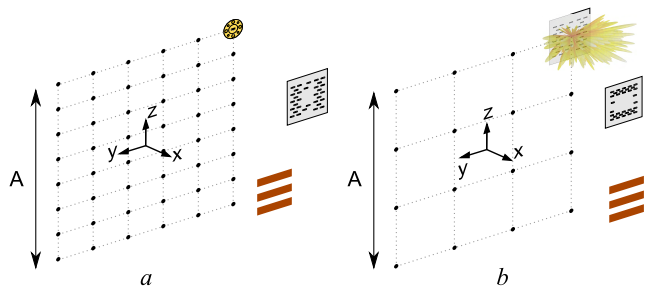
FIGURE 13. *a* Sketch of OEWG to cavity imaging scenario with the OEWG scanned over the area of the aperture, *b* Sketch of the cavity to cavity imaging scenario and an example of the radiation pattern of the cavity at 92.5 GHz.

The sketch of both cavity imaging scenarios is shown in Fig. 13. The experiments are identical to the setup of the OEWG imaging scenario in Fig. 1 in terms of scan area size A, distance of the fixed Rx head to the origin of the scan area P_0, and target distance R. The input power at the feeding port is also identical to the previous experiment (10 dBm). The radiation efficiency of the OEWG antennas is close to 1 throughout

the entire spectrum. Due to the high Q-factor and material surface roughness, the radiation efficiency of the cavity is on average 0.36 (measured using near-field scan and compared to the standard-gain horn with known radiation efficiency). Even with round-trip path loss (for $R = 15$ cm target offset) on the order of 60 dB, the dynamic range of the PNA combined with the robustness of the computational approach will render desired images. The measurements are performed by consecutively moving the extension head attached to the moving stage within a rectangular grid of 15×15 cm to synthesize the apertures illustrated in Fig. 13a and 13b. At each point, one of the heads transmits and the other receives the waveform reflected from the target in the scene, which is at an offset of 15 cm (consistent with the OEWG to OEWG experiment). The recorded reflected signal is the S_{21} parameter measured by the network analyzer. The 5 mm resolution target and the five square 5 mm points (Fig. 2a and c) were imaged as in the previous experiments.

Before any measurements can be performed, it is necessary to perform a precise phase calibration and alignment procedures to achieve imaging results. This includes phase calibration of the feeding network [33] to bring the measurement reference plane to the output flanges of the W-band extension heads. A standard phase calibration procedure is followed using open, short, and matched load standards, over the bandwidth of interest (calibration kit Agilent W11644A).

The spatial alignment of the measurement setup is necessary due to the highly varying fields of the cavities (example in Fig. 13b). We note that when we initially switched to the cavity to cavity scenario (Fig. 13b), we were not able to obtain any images of the targets using the simple alignment techniques used for the purely OEWG based setup (Fig. 1b). Even a very small misalignment, in the range of millimeters for translation or one degree of rotation, caused the reconstruction of the image to break. As reported in [30], misalignment effects have been studied for imaging systems working in the K-band (18 - 26.5 GHz). At W-band, the sensitivity of the imager is amplified four times due to increased frequency of operation.

To perform the alignment, the radiated fields and the physical position of the cavities were related through the correlation of optical and RF fiducials built into the antennas. The optical fiducials consisted of reflector stickers placed on the surface of the antenna. Their locations were obtained using a commercial stereo photogrammetry device, MaxSHOT (CREAform). The RF fiducials consisted of specific radiating slots positioned outside the Mills Cross pattern to distinguish them easily in the nearfield scans. To locate the RF fiducials, the magnitude of the fields (summed over the full bandwidth) were back-propagated to the plane of the aperture. Knowledge of the positions of optical fiducials with respect to the RF fiducials then enabled the alignment of the two coordinate systems using appropriate transformation matrices [34]. While it would be ideal to scan the location of the optical fiducials for each position of the scanning head in the synthesized aperture, the precision of the scanner (NSI -100V-1x1)

on the order of 0.05 mm allowed us to use the initial position scan and set up a rectangular grid of measurement points for successful imaging.

Once the phase calibration and alignment of the fields of the antennas with respect to their physical position was done, imaging could be performed. As suggested by the singular value spectrum in Fig. 14, we should need fewer measurements, compared to the OEWG to OEWG experiment to obtain images of similar quality. This reduction in the number of required measurement modes was demonstrated in practice, with 48 positions (resulting in 48 synthesized Tx antennas and one fixed Rx antenna) which gives $M = 48 \times 200 = 9600$ measurements (compared to 24200 measurements of the first setup) producing the images shown in Fig. 15b and d on a grid of $N = 140 \times 140 = 19600$ pixels. Note that a rectangular grid of six vertical and eight horizontal measurement points is formed resulting in 2.5 cm vertical, and 1.875 cm horizontal sampling distance of the same 15×15 cm aperture A.

Replacing the other OEWG by the resonant cavity (see Fig. 13b), and again applying the alignment method described previously, it was shown that 16 positions (forming four times four rectangular measurement points grid with 3.75 cm ($11\lambda_c$) sampling in both vertical and horizontal directions over the same aperture size; 16 Tx and 1 Rx antenna) resulting in $M = 16 \times 200 = 3200$ measurements (considering 200 frequency points) was enough to produce the images in Fig. 16b and d over a grid of $140 \times 140 = 19600$ pixels.

Despite the radiation efficiency of the cavity is lower than we designed it to be, there is good agreement between the images reconstructed using the OEWG and the frequency diverse approaches [12], [15]. However, a slight degradation in the image quality can be observed in the frequency diverse case. As described above, the predominant contributor to the effective noise is the incompleteness of the measurement modes, which allow reconstruction only of a best estimate of the scene. Since we have incomplete mode coverage in all cases, we see limited resolution and reconstruction error in all of the images. Once this main source of error has been identified, then several additional factors contributing to image quality can be identified: precision of the mechanical alignment; sparse sampling of spatial frequencies; and assumptions made in the forward model, which considers only the first order reflections from the target (Born approximation). We now consider each contribution in more detail.

Alignment precision has been documented to be crucial to the operation of the frequency diverse approaches at K-band [15], [16], [30]. Approximately four times higher sensitivity of W-band system to misalignments compared to the results in [34] suggests that the translation and rotational uncertainty is on the order of $\lambda_c/25$ and <0.5 deg respectively. Added to the precision of the translation stage (NSI-100V-1x1) on the order of 0.02 - 0.05 mm RMS [35], the final translation uncertainty is 0.148 - 0.178 mm RMS, or $\lambda_c/21 - \lambda_c/18$ RMS.
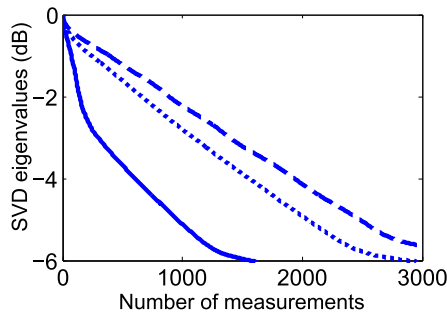
FIGURE 14. Singular value spectrums of all three experimental setups considering the same ROI and an equal number of measurements indicating improving the information content of the measurements. The data was obtained from Virtualizer simulation using near-field scans of the antennas. The full line is the SVD spectrum for OEWG to OEWG scenario, the dotted one of OEWG to the cavity, and dashed of the cavity to cavity scenario.

With a limited number of measurement modes, the spatial frequency bandwidth cannot be uniformly covered, leading to information being lost in the reconstruction. Increasing the number of measurement modes can improve the situation, so long as the modes are spatially distinct. SAR provides an ideal set of measurements as the aperture is sampled uniformly at half wavelength intervals, and thus provides datasets for optimal diffraction-limited imaging performance. The frequency-diverse systems can approach SAR quality [15], [16], but by heavily oversampling the scene to compensate for the inherent redundancy in the modes. Alternatively, compressive sensing approaches can be used to improve reconstructions through the use of intelligent assumptions about the missing information.

The adequacy of the first order Born approximation used in the Virtualizer simulations [12] is reasonable in light of our experimental setup. The radiated energy (random radiation pattern of the cavities) is spread over a volume much larger than the the volume of the target with no other scattering bodies present in the scene. Therefore, the influence of higher order reflections is considered minimal. Background measurements have been performed and subtracted from the target measurements to further diminish the possible aliasing by the residual reflections from the RF absorber surrounding the setup.
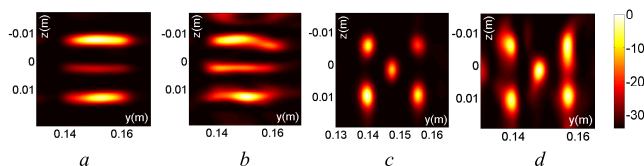

FIGURE 15. Comparison of simulated (*a* and *c*) experimental (*b* and *d*) imaging results of the same targets as in Fig. 2 using OEWG to cavity setup (Fig. 13a).

The simulation results in Fig. 15a, b, and 16a, b assume perfect alignment of the panels and their radiated fields and represent the best possible image fidelity for the setup utilizing 48 and 16 positions.
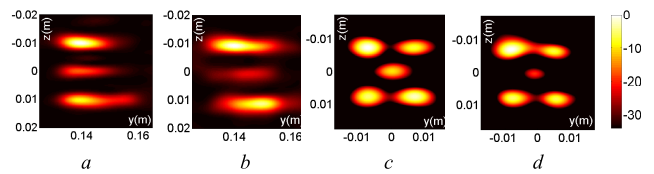
FIGURE 16. Comparison of simulated (*a* and *c*) and experimental (*b* and *d*) imaging results of the same targets as in Fig. 2 using cavity to cavity setup (Fig. 13b).

In order to obtain images of similar fidelity as in Fig. 2, increasing the number of measurements can bring an improved result at the expense of the duration of measurement. We seek only an initial demonstration at W-band, here, and not to fully quantify the large trade-off space or determine the resolution limit of the setup [25].
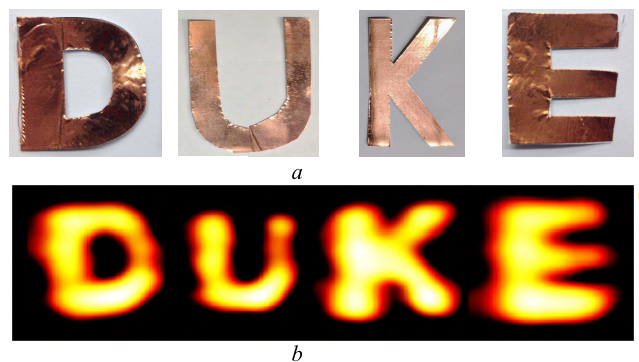
FIGURE 17. *a* Photograph of a DUKE letters cut from a copper tape, the height of the letters is 5 cm, *b* result of imaging the sign (a complex target from the imaging point of view) using the cavity to cavity setup. Each letter was imaged separately due to the small size of the aperture.

To test the imaging capability of the cavity to cavity setup, we constructed a set of letters spelling the word "DUKE" (with 5 cm font size) from a copper adhesive tape and used it as a test target, as shown in Fig. 17a. Imaging the whole sign at once was difficult due to the small aperture size (15 × 15 cm) and the available measurements capacity (we used 16 measurements as in the last experiment). Instead, we imaged each letter separately. The final stitched image of the sign is shown in Fig. 17b where each letter is clearly recognized.

Although these imaging scenarios are synthesized using a moving stage, commercially available solid-state frequency up and down-converters are a path to fully electronic frequency diverse imaging at W-band and constitute a subject of future research.

VI. CONCLUSION

We presented a frequency-diverse imaging scheme at W-band leveraging resonant cavities for standoff security screening and other relevant applications. Experiments have shown that the frequency diverse scheme offers a considerable reduction of the number of measurements positions needed for imaging, compared with MIMO setups utilizing basic

waveguide antennas. This directly translates in hardware savings in terms of the price of the whole system. In utilizing this approach, one must adapt to the challenges of utilizing highly spatially varying radiation patterns, which include the necessity for accurate alignment procedures. However, as we have shown, it is possible to develop robust methods that address these challenges.

ACKNOWLEDGMENT

REFERENCES

[1] V. Mikla, "The use of X-rays for medical purposes," in *Medical Imaging Technology*. Dordrecht, The Netherlands: Elsevier, 2013, ch. 1.5.

[2] M. Hurtado and A. Nehorai, "Polarimetric detection of targets in heavy inhomogeneous clutter," *IEEE Trans. Signal Process.*, vol. 56, no. 4, pp. 1349–1361, Apr. 2008, doi: 10.1109/TSP.2007.909046.

[3] A. M. Florini, "The opening skies: Third-party imaging satellites and us security," *Int. Secur.*, vol. 13, no. 2, pp. 91–123, 1988.

[4] D. A. Pritchard, "An infrared imaging area sensor for tactical and physical security applications," Sandia Nat. Lab., Albuquerque, NM, USA, Tech. Rep. SAND-90-0494 ON: DE90016689, 1990.

[5] S. S. Ahmed, "Microwave/mm-Wave imaging systems," presented at the IEEE Bi-Polar/BiCMOS Circuits Technol. Meeting, Sep./Oct. 2013, doi: 10.1109/BCTM.2013.6798142.

[6] S. S. Ahmed, A. Schiessl, and L.-P. Schmidt, "A novel fully electronic active real-time imager based on a planar multistatic sparse array," *IEEE Trans. Microw. Theory Techn.*, vol. 59, no. 12, pp. 3567–3576, Dec. 2011, doi: 10.1109/TMTT.2011.2172812.

[7] L. Crutona and M. I. Skolnik, "Synthetic aperture radar," in *Radar Handbook*, 3rd ed. New York, NY, USA: McGraw Hill, 1990, ch. 17.

[8] R. Körber, V. Ziegler, and U. Schmid, "Imaging millimeter wave radar with phased array antenna," in *Advanced Microsystems for Automotive Applications*. Berlin, Germany: Springer, 2008, pp. 167–180.

[9] D. M. Sheen, D. L. McMakin, and T. E. Hall, "Three-dimensional millimeter-wave imaging for concealed weapon detection," *IEEE Trans. Microw. Theory Techn.*, vol. 49, no. 9, pp. 1581–1592, Sep. 2001.

[10] S. Venkatesh, N. Viswanathan, and D. Schurig, "W-band sparse synthetic aperture for computational imaging," *Opt. Express*, vol. 24, no. 8, pp. 8317–8331, 2016.

[11] T. Fromenteze *et al.*, "Computational imaging using a mode-mixing cavity at microwave frequencies," *Appl. Phys. Lett.*, vol. 106, no. 19, p. 194104, 2015, doi: 10.1063/1.4921081.

[12] O. Yurduseven, V. R. Gowda, J. N. Gollub, and D. R. Smith, "Printed aperiodic cavity for computational and microwave imaging," *IEEE Microw. Wireless Compon. Lett.*, vol. 26, no. 5, pp. 367–369, May 2016, doi: 10.1109/LMWC.2016.2548443.

[13] D. J. Brady, "Coded aperture and tomographic imaging," in *Optical Imaging and Spectroscopy*. Hoboken, NJ, USA: Wiley, 2008, ch. 1.

[14] J. Hunt *et al.*, "Metamaterial apertures for computational imaging," *Science*, vol. 339, no. 6117, pp. 310–313, Jan. 2013, doi: 10.1126/science.1230054.

[15] O. Yurduseven, J. N. Gollub, A. Rose, D. L. Marks, and D. R. Smith, "Design and simulation of a frequency-diverse aperture for imaging of human-scale targets," *IEEE Access*, vol. 4, pp. 5436–5451, 2016, doi: 10.1109/ACCESS.2016.2604823.

[16] J. N. Gollub *et al.*, "Large metasurface aperture for millimeter wave computational imaging at the human-scale," *Sci. Rep.*, vol. 7, Feb. 2017, Art. no. 42650.

[17] T. Zvolensky, J. N. Gollub, D. L. Marks, and D. R. Smith, "Design and analysis of a W-band metasurface-based computational imaging system," *IEEE Access*, vol. 5, pp. 9911–9918, May 2017, doi: 10.1109/ACCESS.2017.2703860.

[18] D. Paganin, "Coherent X-ray imaging," in *X-Ray Optics*. Oxford, U.K.: Oxford Univ. Press, 2006, ch. 4.

[19] S. S. Ahmed, *Electronic Microwave Imaging With Planar Multistatic Arrays*. Berlin, Germany: Logos, 2014.

[20] A. Boag, "A fast multilevel domain decomposition algorithm for radar imaging," *IEEE Trans. Antennas Propag.*, vol. 49, no. 4, pp. 666–671, Apr. 2001.

[21] G. Lipworth *et al.*, "Comprehensive simulation platform for a metamaterial imaging system," *Appl. Opt.*, vol. 54, no. 31, pp. 9343–9353, 2015.

[22] D. Schurig, J. J. Mock, and D. R. Smith, "Electric-field-coupled resonators for negative permittivity metamaterials," *Appl. Phys. Lett.*, vol. 88, no. 4, p. 041109, 2006, doi: doi.org/10.1063/1.2166681.

[23] C. A. Balanis, "Dyadic green's functions," in *Advanced Engineering Electromagnetics*, 2nd ed. Hoboken, NJ, USA: Wiley, 2012, ch. 15, sec. 7, pp. 938–940.

[24] P. M. Woodward, "Simple theory of radar reception," in *Probability and Information Theory, With Applications to Radar*. Amsterdam, The Netherlands: Elsevier, 1953.

[25] O. Yurduseven *et al.*, "Resolution of the frequency diverse metamaterial aperture imager," *Prog. Electromagn. Res.*, vol. 150, pp. 97–107, Jan. 2015, doi: 10.2528/PIER14113002.

[26] L. C. Potter, E. Ertin, J. T. Parker, and M. Cetin, "Sparsity and compressed sensing in radar imaging," *Proc. IEEE*, vol. 98, no. 6, pp. 1006–1020, Jun. 2010, doi: 10.1109/JPROC.2009.2037526.

[27] V. N. Nguyen, "Design, analysis, and characterization of metamaterial quasi-optical components for millimeter-wave automotive radar," Ph.D. dissertation, Dept. Elect. Eng. Comput., Duke Univ., Durham, NC, USA, 2013.

[28] M. Bozzi, A. Georgiadis, and K. Wu, "Review of substrate-integrated waveguide circuits and antennas," *IET Microw. Antennas Propag.*, vol. 5, no. 8, pp. 909–920, Jun. 2011, doi: 10.1049/iet-map.2010.0463.

[29] S. Gregson, J. McCormick, and C. Parini, "Introduction to near-field antenna measurements," in *Principles of Planar Near-Field Antenna Measurements*, 1st ed. Edison, NJ, USA: IET, Dec. 2007, ch. 3, pp. 35–60.

[30] H. Odabasi, M. F. Imani, G. Lipworth, J. N. Gollub, and D. R. Smith, "Investigation of alignment errors on multi-static microwave imaging based on frequency-diverse metamaterial apertures," *Prog. Electromagn. Res. B*, vol. 70, pp. 101–112, Oct. 2016.

[31] D. L. Marks, J. Gollub, and D. R. Smith, "Spatially resolving antenna arrays using frequency diversity," *J. Opt. Soc. Amer. A, Opt. Image Sci.*, vol. 33, no. 5, pp. 899–912, 2016, doi: 10.1364/JOSAA.33.000899.

[32] D. M. Pozar, "Transmission lines and waveguides," in *Microwave Engineering*, 4th ed. Hoboken, NJ, USA: Wiley, 2011, ch. 3, sec. 3.3, pp. 110–120.

[33] O. Yurduseven, J. N. Gollub, K. P. Trofatter, D. L. Marks, A. Rose, and D. R. Smith, "Software calibration of a frequency-diverse, multistatic, computational imaging system," *IEEE Access*, vol. 4, pp. 2488–2497, May 2016, doi: 10.1109/ACCESS.2016.2570678.

[34] T. Sleasman *et al.*, "Near field scan alignment procedure for electrically large apertures," *IEEE Trans. Antennas Propag.*, vol. 65, no. 6, pp. 3257–3262, Jun. 2017, doi: 10.1109/TAP.2017.2691465.

[35] NSI Online Data Sheet. *Small Vertical XY Positioners*. [Online]. Available: https://www.nsi-mi.com/products/mechanical-products/linear-positioners/small-vertical-xy-positioners

TOMAS ZVOLENSKY received the M.Sc. degree in radio science and engineering from the Brno University of Technology, Brno, Czech Republic, in 2008, and the Ph.D. degree in radio science and engineering from Aalto University, Espoo, Finland, in 2014. Since 2016, he has been with a startup company Teraphic, a part of research and development and business development commercializing 3-D printing technologies for millimeter-wave applications. His main research interests include metamaterials, leaky-wave antennas, composite CRLH structures, tunable millimeter-wave antennas and devices, development of imaging capabilities of meta-surfaces in millimeter-wave range, and targeting security imaging applications.

VINAY R. GOWDA received the B.E. degree in electrical and communication engineering from Visvesvaraya Technological University, Karnataka, India, in 2009, and the M.S. degree in electrical engineering from The University of Texas, Arlington, TX, USA, in 2011. From 2011 to 2014, he was a Hardware Engineer with Intel/Intel Labs, Folsom, CA, USA. Since 2014, he has been with the Center for Metamaterials and Integrated Plasmonics, Duke University, Durham, NC, USA. He is currently a Graduate Student with the Department of Electrical and Computer Engineering. His current research interests include wireless power transfer, focused apertures, metamaterials, and RF design.

JONAH GOLLUB (M'16) received the B.A. degree in physics from Reed College in 2000 and the Ph.D. degree in physics from the University of California at San Diego, San Diego, CA, USA, in 2009. His thesis was on characterizing the hybridization of metamaterials with magnetic materials. From 2010 to 2012, he was a Lead Modeling and Simulation Scientist with a startup company, where he was involved in developing surface meta-materials with applications targeted toward imaging and biological detection under DARPA, MDA, Army, and NSF funded efforts. He joined Duke University as a Research Scientist in 2013, where he is currently focused on developing real-time millimeter-wave imaging approaches, which utilize frequency diverse antennas and compressive imaging techniques.

DANIEL L. MARKS was born in Chicago, IL, USA, in 1973. He received the B.S., M.S., and Ph.D. degrees from the University of Illinois at Urbana, Champaign, IL, USA, in 1995, 1998, and 2001, respectively. From 2001 to 2008, he was a Research Scientist with the Biophotonics Laboratory, University of Illinois at Urbana. He has been an Associate Research Professor with the Department of Electrical and Computer Engineering, Duke University, since 2009. He has authored 85 research articles and holds 17 patents. His research interests include optics, optical design, computational imaging, millimeter-wave and terahertz imaging, metamaterials, and synthetic electromagnetic structures. He has been an Editor of *Applied Optics*.

DAVID R. SMITH received the Ph.D. degree in physics from the University of California at San Diego (UCSD), in 1994. He is currently the Department Chair and the James B. Duke Professor of electrical and computer engineering with Duke University and the Director of the Center for Metamaterials and Integrated Plasmonics. He is also an Adjunct Professor with the Physics Department, UCSD, an Affiliate Faculty Member with the Electrical and Computer Engineering Department, University of Washington, and a Visiting Professor of physics with the Imperial College London, London. His research interests include the theory, simulation, and characterization of unique electromagnetic structures, including photonic crystals and metamaterials, and the applications of such materials.

He and his colleagues demonstrated the first left-handed (or negative index) metamaterial at microwave frequencies in 2000 while at UCSD. He has authored over 200 publications on matematerials and plasmonics. In 2002, he was elected as a member of the Electromagnetics Academy. In 2005, he was part of a five-member team that received the Descartes Research Prize by the European Union for their contributions to metamaterials and other novel electromagnetic materials. He received the Stansell Research Award from the Pratt School of Engineering, Duke University, in 2005. In 2006, he was selected as one of the Scientific American 50, a group recognized by the editors of *Scientific American* for achievements in science, technology, and policy. His work has appeared twice on the cover of *Physics Today*, and twice has been selected as one of the Top Ten Breakthroughs of the year by the *Science Magazine*. In 2013, he was a co-recipient of the James C. McGroddy Prize for New Materials by the American Physical Society. He was selected by the ISI-Reuters as a Citation Laureate in 2009, for the most number of highly cited papers in physics over the last decade. He was once again recognized as one of the Highly Cited Researches 2014 by ISI-Reuters in the category of physics. In 2006, he along with his colleague Prof. J. Pendry, suggested metamaterials could be used to design an electromagnetic cloak, introducing the new design tool of transformation optics. In 2013, he was asked to write an op-ed piece for *The New York Times* on cloaking research. He served as the Founding and the Acting Director of the Metamaterials Commercialization Center, a unit within the Intellectual Ventures, Bellevue, WA, USA, in 2013, dedicated to commercializing metamaterials concepts. MCC has thus far produced three spin out companies: Kymeta Corporation, Redmond, WA, USA; Evolv Technologies, Waltham, MA, USA; and Echodyne, Bellevue. He is a Co-Founder of Evolv Technologies, which targets metamaterial apertures for security screening applications, and Echodyne, which is seeking to apply metamaterial apertures to radar applications. He serves on the Advisory Board for Kymeta, which targets metamaterial-based antennas for satellite communications.

• • •